Mixing events in a stratified jet subject to surface wind and buoyancy forcing

Hieu T. Pham and Sutanu Sarkar†

Mechanical and Aerospace Engineering, University of California, San Diego, La Jolla, CA 92093, USA

The fine-scale response of a subsurface stable stratified jet subject to the forcing of surface wind stress and surface cooling is investigated using direct numerical simulation. The initial velocity profile consists of a symmetric jet located below a surface layer driven by a constant wind stress. The initial density profile is well-mixed in the surface layer and linearly stratified in both upper and lower flanks of the jet. The minimum value of the gradient Richardson number in the upper flank of the jet exceeds the critical value of 0.25 for linear shear instability. Broadband finite-amplitude fluctuations are introduced to the surface layer to initiate the simulation. Turbulence is generated in the surface layer and deepens into the jet upper flank. Internal waves generated by the turbulent surface layer are observed to propagate downward across the jet. The momentum flux carried by the waves is significantly smaller than the Reynolds shear stress extracted from the background velocity. The wave energy flux is also smaller than the turbulence production by mean shear. Ejections of fluid parcels by horseshoe-like vortices cause intermittent patches of intense dissipation inside the jet upper flank where the background gradient Richardson number is larger than 0.25. Drag due to the wind stress is smaller than the drag caused by turbulent stress in the flow. Analysis of the mean and turbulent kinetic energy budgets suggests that the energy input by surface forcing is considerably smaller than the energy extracted from the initially imposed background shear in the surface layer.

Key words: ocean processes, stratified turbulence

1. Introduction

Many environmental flows have jet-like velocity profiles, such as the equatorial undercurrents (EUCs) and the equatorial deep jets in the ocean, and the tropospheric jet in the atmosphere. These jets occur in a background with non-uniform continuous stratification. Observations (Gregg *et al.* 1985; Moum *et al.* 1992; Lien, McPhaden & Gregg 1996), linear stability analysis (Sun, Smyth & Moum 1998), two-dimensional simulations (Skyllingstad & Denbo 1994; Smyth & Moum 2002; Sutherland 2006), and three-dimensional large eddy simulations (Wang, McWiliams & Large 1998; Wang & Muller 2002) have been utilized to study aspects of these flows. However, there are only a handful of studies using three-dimensional (3D) direct numerical simulation (DNS) (Tse *et al.* 2003; Pham & Sarkar 2010*a*) in which all scales of motion are

† Email address for correspondence: ssarkar@ucsd.edu

resolved. In the current study, 3D-DNS will be utilized to investigate the fine-scale response of a stratified jet subject to surface wind stress and buoyancy forcing.

The EUCs, jet-like eastward flows below westward surface currents, play an important role in the balance of the equatorial heat budget. It is believed that variability in the EUCs can affect the surface temperature, modulate air/sea coupling, and thereby affect weather patterns (Philander 1980). Therefore, it is important to understand and ultimately quantify the fine-scale processes in the EUCs. Observations in the Pacific EUC have shown nightly occurrences of intermittent highly dissipative turbulence patches along with narrowband high-frequency oscillations in the EUC upper flank where the background gradient Richardson number is larger than the critical value of 0.25 for linear shear instability. However, the mechanism responsible for these dissipative patches remains unclear. One possible explanation is that, at night, the deepening of the surface layer allows formation of a shear-unstable region. Another possible explanation is that the high-frequency oscillations are gravity waves which overturn in the high shear region of the jet. Hebert *et al.* (1992) has recorded an overturning of a wave packet; nonetheless, in a recent study Smyth, Moum & Nash (2010) apply linear stability analysis to the observed mean background velocity and density to infer that the oscillations could result from instabilities that are unrelated to gravity waves. In our previous work (Pham & Sarkar 2010*a*), we find that Kelvin–Helmholtz instabilities associated with an unstable shear region above a stable stratified jet lead to both internal waves and patches of turbulent dissipation. The patches are associated with horseshoe vortices originating from the unstable shear layer and not breaking internal waves.

A number of studies have used two-dimensional simulations to investigate dynamical processes inside the EUC jets. The first two-dimensional simulation performed by Skyllingstad & Denbo (1994) using field-observed velocity and density profiles, surface wind stress and heat flux showed the presence of internal waves propagating downward and upstream. The waves are suggested to be related to Kelvin–Helmholtz instability; however, no patches of dissipation are observed and wave breaking is not discussed. Smyth & Moum (2002) perform simulations of a Bickley jet which has stratification in the upper flank weaker than that in the lower flank. With the low stratification, shear instability in the upper flank is allowed resulting in the formation of vortex structures. Internal waves are observed to propagate from the upper flank to the lower flank where they break after encountering a critical layer. Although not specifically targeting the EUCs, the simulations of Sutherland (2006) also show that internal waves can be generated when a portion of a jet is linearly unstable such that vortex structures are formed. Nonetheless, the formation of vortex structures with vertical extent as large as the jet thickness in those simulations is not applicable to the observation of turbulence limited to the upper flank of the EUCs. Discussion of turbulence inside the jet is absent in the aforementioned two-dimensional studies.

A 3D-DNS motivated by turbulence in the tropospheric jet was carried out by Tse *et al.* (2003). The jet is weakly stratified and the background shear is maintained by forcing. Turbulence is observed in the core of the jet while nonlinear waves are observed at the edges of the jet. In a subsequent study where numerical viscosity is used, Mahalov *et al.* (2007) find propagating waves in the region above the jet when the stratification there is increased. Since Tse *et al.* (2003) and Mahalov *et al.* (2007) did not intend to study the EUCs, the background conditions of the simulations are different and the simulated turbulence in the jet deviates from EUC observations. Pham & Sarkar (2010*a*) perform 3D-DNS to investigate a linearly stable

stratified jet adjacent to a linearly unstable shear layer. The shear layer is subject to Kelvin–Helmholtz shear instability. Internal waves are observed to propagate upstream and downward from the shear layer across the jet toward the region below. Intermittent highly dissipative patches of turbulence are observed in the jet upper flank where the gradient Richardson number is larger than 0.25. The turbulence patches are found to correlate with horseshoe-like vortex structures formed inside the Kelvin–Helmholtz rollers that extend downward deep inside the jet.

All the studies targeting the EUCs mentioned above have been helpful to decipher the small-scale dynamical process in the EUCs and related stratified shear flows but at the same time important questions remain unanswered. For example, (i) previous studies have shown that internal waves are strongly related to large-scale vortex structures that result from shear instability in a small region of the jet. Can internal waves be found inside the jet in the absence of such large-scale vortex structures? (ii) Pham & Sarkar (2010a) have indicated that the turbulence inside the jet is driven by the formation of horseshoe vortices which originate from a spanwise instability of Kelvin–Helmholtz rollers. Can similar vortex structures be formed in the absence of the large-scale Kelvin–Helmholtz rollers? (iii) Except in Skyllingstad & Denbo (1994), most studies have assumed some form of shear instability inside the jet neglecting the turbulent mixed layer. What role does surface forcing of the mixed layer play relative to shear instability inside the jet? In this study, we will address these issues by using 3D-DNS to investigate the interaction of a surface layer driven by a constant wind stress and surface cooling with a linearly stable stratified jet.

2. Problem formulation

Consider a subsurface jet with peak velocity U_j and thickness δ_0 centred at $z = -(5/3)\delta_0$:

$$\langle u_j \rangle (z) = U_j \exp \left[-\left(\frac{z + (5/3)\delta_0}{\delta_0} \right)^4 \right], \tag{2.1}$$

where the brackets $\langle \cdot \rangle$ indicate horizontal x–y average. A free surface shear layer of thickness $\delta_m = \delta_0/3$ driven by a constant wind stress of $\tau_w = -6.67 \times 10^{-4} \rho_0 U_j^2$ with the following profile:

$$\langle u_w \rangle (z) = -1.76 U_j \left\{ \left(1 + 2 \left(\frac{z}{\delta_m} \right)^2 \right) \operatorname{erfc} \left(\frac{z}{\delta_m} \right) - \frac{2}{\pi} \frac{z}{\delta_m} \exp \left[-\left(\frac{z}{\delta_m} \right)^2 \right] \right\}, \tag{2.2}$$

is added to the jet velocity. Here, ρ_0 is a reference density. The negative sign of the wind stress indicates that the wind blows opposite to the jet. The exerted wind stress corresponds to the frictional velocity $u_\tau = \sqrt{(\tau_w/\rho_0)} = 0.026 U_j$. The complete initial velocity profile $\langle u \rangle = \langle u_j \rangle + \langle u_w \rangle$ is shown in figure 1(a).

The vertical density profile consists of a well-mixed surface layer that transitions to a linearly stratified jet region and the region below. The corresponding non-dimensional stratification profile, $J(z) = N^2 \delta_0^2 / U_j^2$, is given by

$$J(z) = \frac{J_j}{2} - \frac{J_j}{2} \tanh \left(\frac{z + \delta_m}{0.5 \delta_m} \right), \tag{2.3}$$

where $N^2 = -(g/\rho_0) \, \mathrm{d}\langle \rho \rangle / \mathrm{d}z$ is the squared buoyancy frequency, g is gravity, and J_j is a measure of stratification in the jet layer that is set to 0.68. The initial mean profiles
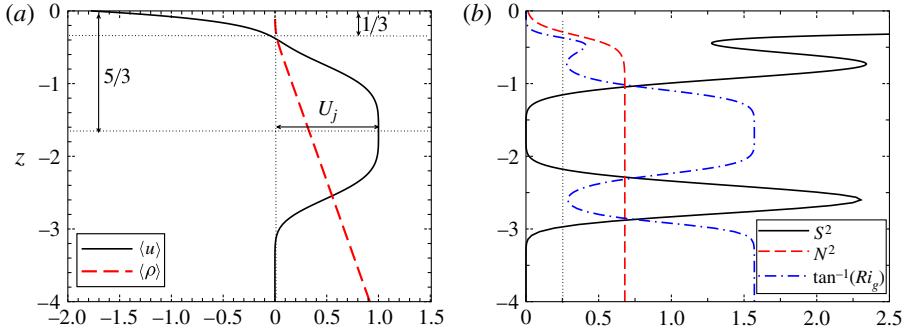
FIGURE 1. (Colour online available at journals.cambridge.org/flm) (a) Initial mean profiles. The velocity profile consists of a stratified jet below a wind-driven mixed layer. The jet centre is at depth $z = -(5/3)\delta_0$. (b) Initial squared shear profile S^2, squared buoyancy frequency profile N^2 normalized by U_j^2/δ_0^2, and gradient Richardson number profile Ri_g. The vertical dotted line indicates the critical value $Ri_g = 0.25$ for shear instability. Thus, only the thin surface region, $-0.33 < z < 0$, has linearly unstable shear.

of S^2, J and Ri_g are shown in figure 1(b). $Ri_g < 0.25$ only in a thin surface region $-0.33 < z < 0$ and $Ri_g > 0.25$ everywhere in the jet and the region below. A constant surface cooling of $Q_s = 3.87 \times 10^{-5} U_j^3/\delta_0$ is imposed at $z = 0$.

Using δ_0, U_j and $\delta_0 \, \mathrm{d}\langle\rho\rangle/\mathrm{d}z|_{-\infty}$ as the characteristic length, velocity and density, the non-dimensional, non-hydrostatic governing equations with the Boussinesq approximation are:

$$\frac{\partial u_k}{\partial x_k} = 0, \tag{2.4}$$

$$\frac{\partial u_i}{\partial t} + \frac{\partial (u_k u_i)}{\partial x_k} = -\frac{\partial p}{\partial x_i} + \frac{1}{Re}\frac{\partial^2 u_i}{\partial x_k \partial x_k} - J_j \rho' \delta_{i3}, \tag{2.5}$$

$$\frac{\partial \rho}{\partial t} + \frac{\partial (u_k \rho)}{\partial x_k} = \frac{1}{Re\,Pr}\frac{\partial^2 \rho}{\partial x_k \partial x_k}. \tag{2.6}$$

The non-dimensional parameters are Reynolds number $Re = U_j \delta_0/\nu$ and Prandtl number $Pr = \nu/\kappa$, where ν is the kinematic viscosity and κ is the thermal diffusivity, respectively. It should be noted that p is the dynamic pressure and ρ does not include the reference density ρ_0 as shown in figure 1. Hereafter, all parameters are discussed in non-dimensional units. In the current study, $Re = 18\,000$ while $Pr = 1$. The Reynolds number, $Re_\tau = u_\tau \delta_m/\nu$, based on the wind stress is 156. Table 1 compares the imposed non-dimensional parameters to those observed in the field. Although the values of Ri_g are similar, the jet Reynolds numbers and non-dimensional heat flux are significantly smaller in the DNS. In the DNS, while all scales of motion are resolved, the dimensional flow properties are different from corresponding values in observations.

The initial velocity perturbations have a broadband spectrum given by

$$E(k) \propto \left(\frac{k}{k_0}\right)^4 \exp\left[-2\left(\frac{k}{k_0}\right)^2\right], \tag{2.7}$$

Parameter	Observation	Current study
U_j	1 m s^{-1}	
δ_0	80 m	
δ_m	20 m	
N^2	1.3×10^{-4} s^{-2}	
S^2	4.2×10^{-4} s^{-2}	
τ_w	-0.02 N m^{-2}	
u_τ	0.0045 m s^{-1}	
Q_s	6.4×10^{-8} W kg^{-1}	
Ri_g	0.31	0.43
Pr	7	1
Re	8×10^7	1.8×10^4
Re_τ	8.9×10^4	156
$Q_s \delta_m / u_\tau^3$	14.0	0.75

TABLE 1. Comparison of non-dimensional parameters between simulations and observations. Observational data in the first column are taken from Moum *et al.* (1992) in which the jet centre velocity is U_j, the jet thickness is δ_0 and mixed layer depth is δ_m. Values of N^2, S^2, and Ri_g are measured at depth $z = 28$ m in the observational data while it is computed at $z = -0.5$ in the current study.

where wavenumber k_0 is set such that the spectrum peaks at $5.1\delta_0$. The fluctuations introduced only in the surface layer have root mean square (r.m.s.) values that peak at the surface at (u', v', w') of 7 % U_j and rapidly decrease with depth.

Periodic boundary conditions are used in the streamwise (x) and spanwise (y) directions. Boundary conditions in the vertical direction (z) are set as follows:

$$\frac{\partial u}{\partial z}(z = 0) = Re \, \tau_w, \quad u(z_{min}) = 0, \tag{2.8a}$$

$$\frac{\partial v}{\partial z}(z = 0) = \frac{\partial v}{\partial z}(z_{min}) = 0, \tag{2.8b}$$

$$\frac{\partial p}{\partial z}(z = 0) = \frac{\partial p}{\partial z}(z_{min}) = 0, \tag{2.8c}$$

$$w(z = 0) = w(z_{min}) = 0, \tag{2.8d}$$

$$J(z = 0) = Re \, Pr \, Q_s, \quad J(z_{min}) = J_j. \tag{2.8e}$$

The domain size is $(8/3)\pi \times (2/3)\pi \times 10$ and the grid has $768 \times 256 \times 320$ points. The grid is uniform in the horizontal with spacing of 0.011 in the x-direction and 0.008 in the y-direction. The vertical grid size is stretched from a value of 0.002 at the surface to a value of 0.011 at depth $z = -0.33$. In the region $-1.5 < z < -0.33$ the grid is uniform with spacing of 0.011. Below this region, the grid is mildly stretched at 3 %. Corresponding to the wall unit $\delta^+ = \nu/u^* = 0.0022$, the grid spacing is $5.5\delta^+$ and $4\delta^+$ in the x- and y-directions, respectively. The minimum vertical grid spacing is δ^+ at the surface and $5.5\delta^+$ in the jet upper flank.

A second-order finite-difference method on a staggered grid is used for spatial derivatives and a third-order low-storage Runge–Kutta method is used for time advancement, except for the viscous term which is advanced by a Crank–Nicolson scheme. A sponge region is employed at the bottom boundary ($z < -8.6$) to eliminate spurious wave reflections. The velocities and density in this sponge region are relaxed

by adding to the right-hand side of (2.5) and (2.6) a term of the form

$$-\phi(z)[u_i(x_i, t) - \langle u \rangle_i (z, t = 0)], \tag{2.9a}$$

$$-\phi(z)[\rho(x_i, t) - \langle \rho \rangle (z, t = 0)]. \tag{2.9b}$$

The damping function, $\phi(z)$, increases quadratically from $\phi = 0$ to 1.0. Further details of the numerical method can be found in Basak & Sarkar (2006) and Brucker & Sarkar (2007).

In subsequent sections, the evolution equation for turbulent kinetic energy is used extensively for discussion; therefore, it is convenient to introduce the notation here. The equation is

$$\frac{\mathrm{d}K}{\mathrm{d}t} = P - \varepsilon + B - \frac{\partial T_3}{\partial z}. \tag{2.10}$$

Here, K is the turbulent kinetic energy defined as $K = (1/2)\langle u_i' u_i' \rangle$. The prime indicates deviation from the horizontally averaged quantity as in $u_i' = u - \langle u \rangle$. P is the production rate, defined as

$$P \equiv -\langle u_i' u_j' \rangle \frac{\partial \langle u_i \rangle}{\partial x_j} = -\langle u' w' \rangle \frac{\mathrm{d}\langle u \rangle}{\mathrm{d}z}, \tag{2.11}$$

ε is the dissipation rate, defined as

$$\varepsilon \equiv \frac{2}{Re}\langle s_{ij}' s_{ij}' \rangle \quad \text{where } s_{ij}' = \frac{1}{2}\left(\frac{\partial u_i'}{\partial x_j} + \frac{\partial u_j'}{\partial x_i}\right), \tag{2.12}$$

B is the buoyancy flux, defined as

$$B \equiv -J_j\langle \rho' w' \rangle, \tag{2.13}$$

$\partial T_3/\partial z$ is the transport of turbulent kinetic energy (TKE), defined as

$$T_3 = T_t + T_p + T_v, \tag{2.14}$$

where the turbulent transport T_t is defined as

$$T_t = \tfrac{1}{2}[\langle w'u'u' \rangle + \langle w'v'v' \rangle + \langle w'w'w' \rangle], \tag{2.15}$$

the pressure transport T_p is defined as

$$T_p = \frac{\langle p'w' \rangle}{\rho_0}, \tag{2.16}$$

and the viscous transport T_v is

$$T_v = -\frac{2}{Re}[\langle u's_{31}' \rangle + \langle v's_{32}' \rangle + \langle w's_{33}' \rangle]. \tag{2.17}$$

3. Evolution of the mean flow

As the wind stress and the buoyancy flux are applied at the surface, the mixed layer deepens and turbulence penetrates the jet. Significant changes in profiles of the mean quantities such as velocity and density are observed and discussed in this section. Although the wind exerts a constant momentum flux at the surface at $z = 0$, the surface velocity $\langle u_s \rangle$ rapidly decreases owing to mixing of momentum as shown in figure 2(a). From the beginning of the simulation to $t = 20$, $\langle u_s \rangle$ decelerates by more than 50%.
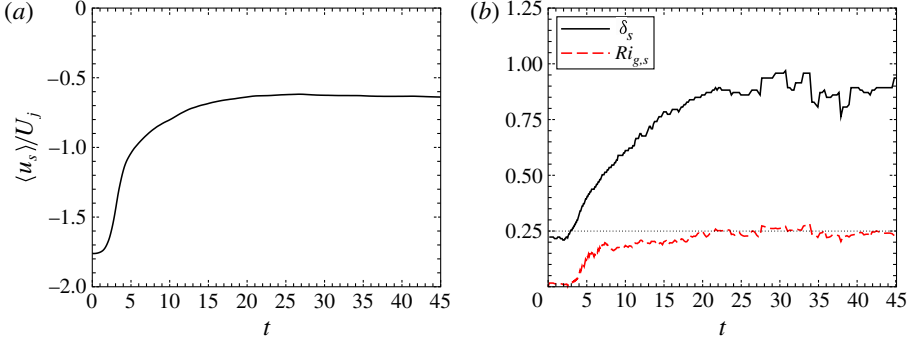
FIGURE 2. (Colour online) Time evolution of (*a*) surface velocity $\langle u_s \rangle$ at $z = 0$, and (*b*) stirring depth δ_s and the corresponding $Ri_{g,s}$. The dotted line indicates the critical value of $Ri_g = 0.25$.

The decrease in $\langle u_s \rangle$ is similar to the results of Tsai, Chen & Moeng (2005). It will be demonstrated later that the rapid initial deceleration is due to the drag caused by the extraction of Reynolds turbulent stress from the mean shear provided in the initial velocity profile $\langle u \rangle$ in the surface layer. Figure 2(*b*) shows the deepening of the surface mixed layer as the simulation progresses. In this figure, δ_s is the stirring depth measured by the distance between $z = 0$ and the stirring boundary defined by the location at which the maximum r.m.s. value of the density fluctuation ρ' is recorded. The initial stirring boundary is located at $z = -0.22$ at the transition between the surface mixed layer and the linearly stratified region below. The simulation is initialized with velocity fluctuations peaking at the surface and decaying with depth. However, stronger velocity fluctuations near the surface do not stir the density field because the background condition is well-mixed. Rather, the peak density fluctuation is observed in the transition region where the density stratification is present despite the weaker velocity fluctuations relative to the region above. After the initial adjustment period $0 < t < 2$, δ_s increases approximately from 0.22 to $0.9\delta_0$ at $t = 20$ and then fluctuates about this value after that. The increase in δ_s signifies the deepening of the turbulence-active mixed layer into the quiescent linearly stratified jet region. The increase of δ_s up to $0.9\delta_0$ also indicates that the turbulence is active in most of the jet upper flank ($-1.67 < z < -0.33$) for $0 < t < 20$. After $t = 20$, stirring, weaker than earlier, continues to occur at the location $z = -\delta_s$ but the turbulence in the region above this location decays except in the thin surface region driven by the wind stress and the surface heat flux. As discussed in a later section, the turbulence generated by the surface forcing is relatively weak compared to that extracted from the mean background velocity. Figure 2(*b*) also shows the values of the gradient Richardson number $Ri_{g,s}$ measured at the stirring boundary $z = -\delta_s$. As δ_s increases, $Ri_{g,s}$ also increases. At $t = 20$ when δ_s ceases to increase, $Ri_{g,s}$ asymptotes at the critical value of 0.25. This suggests that no further stirring can be achieved when the gradient Richardson number exceeds the critical value, which agrees with the prediction of linear stability theory of parallel shear flows.

The profiles of the mean streamwise velocity $\langle u \rangle$ and mean shear S in the surface layer and the jet upper flank at different times are shown in figure 3(*a,b*), respectively. The surface velocity at $z = 0$ decreases initially as discussed above. As the surface layer deepens, the wind stress exerts drag on the layer causing the region with negative velocity to widen. The positive velocity in the upper flank of the jet also decreases
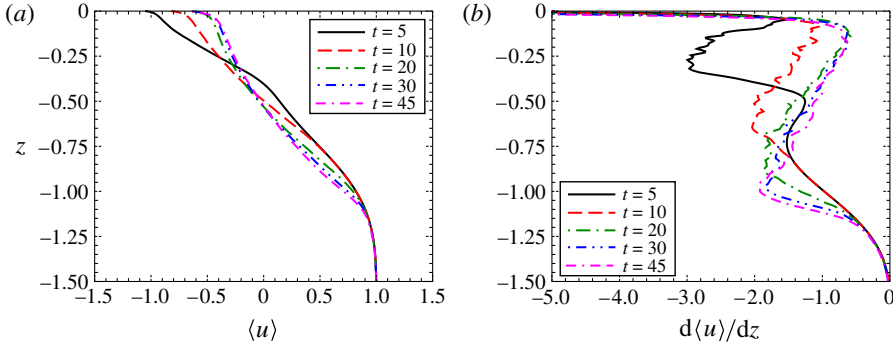
FIGURE 3. (Colour online) Vertical mean profiles at various times: (*a*) streamwise velocity $\langle u \rangle$, (*b*) shear rate $\mathrm{d}\langle u \rangle / \mathrm{d}z$.

in time indicating that a significant amount of momentum is lost from the mean flow. The momentum loss is observed in the jet region as deep as $z = -1.1\delta_0$ where there is insignificant background shear. The profiles of shear S in figure 3(*b*) show significant variations in time except in the thin viscous layer, $-0.1 < z < 0$, at the surface. The initial shear in the surface layer, $-0.33 < z < 0$, is reduced rapidly. From $t = 5$ to $t = 10$, the magnitude of S is reduced by nearly half and continues to decrease after that. In contrast, the shear in the region, $-1.2 < z < -0.75$, of the jet upper flank increases in time although the velocity in this region is reduced as shown in figure 3(*a*). From $t = 5$ to 45 the magnitude of S approximately doubles at depth $z = -1$. The S profile at $t = 5$ consists of two distinct regions of strong shear in addition to the surface shear that are denoted by two local maxima in the profile: one with relatively larger magnitude of S at $z = -0.25$ in the surface layer and one at $z = -0.75$ in the jet upper flank. At the end of the simulation at $t = 45$, the former region disappears while the latter persists with stronger magnitude. The dynamic transformation of the mean velocity and mean shear suggests that the mean background condition has an important role in the momentum and the energy budgets of the flow.

   The evolution of the mean density $\langle \rho \rangle$ and the squared buoyancy frequency N^2 are shown in figure 4(*a,b*), respectively. Except in the thin region near the surface where the density profile is gravitationally unstable due to the positive surface buoyancy flux, the profiles at all time show that the mean density increases with depth. Over time, the surface layer gets heavier and the jet upper flank gets lighter. The stirring of the background density, although co-gradient with the molecular diffusion, is active since the corresponding background shear changes significantly. Neglecting the molecular diffusion effects, the surface layer gets heavier due to two sources: the downward flux due to surface cooling and upward flux due to stirring at the base of the wind-driven layer. The enhanced shear at the base of the wind-driven layer in figure 3(*b*) suggests that the latter dynamical process is related to shear instability. The profiles of N^2 in figure 4(*b*) indicate that the effect of the surface flux is limited to a region as thin as $0.1\delta_0$ near the surface. It should be noted that, by definition, a negative N^2 corresponds to a positive unstable density gradient. The variation among the N^2 profiles is more significant in the region below the surface layer than at the surface. In the surface layer, $-0.33 < z < 0$, the stratification increases in time suggesting that the initial mixed state cannot be maintained despite the surface forcing. In other words, restratification inside the surface layer, even at early time, implies that uplifting of
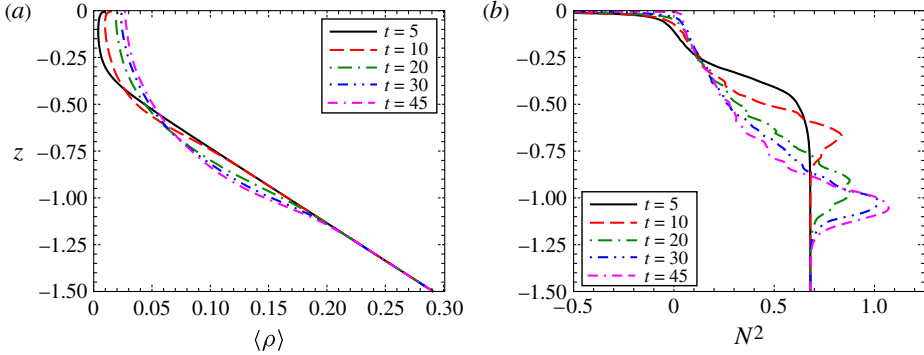
FIGURE 4. (Colour online) Vertical mean profiles at various time: (*a*) density $\langle\rho\rangle$ and (*b*) squared buoyancy frequency N^2.

heavier fluid from the jet upper flank is more important than the downward injection of the positive buoyancy flux at the surface. As the surface layer deepens, the fluid in the region below is stirred resulting in a significant decrease in stratification. For example, from $t = 5$ to 45, the stratification at $z = -0.5$ is reduced by a factor of approximately six. Below the stirring region, N^2 increases sharply to values larger than the ambient value J_j before dropping down toward J_j similar to the observations of the ocean pycnocline capping the surface mixed layer. The overshooting value of N^2 at $z = -1$ and $t = 45$ can be more than $50\,\%$ larger than J_j. The formation of a pycnocline adjacent to a region of active stirring has been observed in other studies such as mixing in a turbulent boundary layer (Taylor & Sarkar 2008; Gayen, Sarkar & Taylor 2010) and mixing via shear instability (Sutherland & Linden 1998; Pham, Sarkar & Brucker 2009).

It is remarkable that, despite significant variations in the shear and squared buoyancy profiles both in time and in space, the values of the gradient Richardson number profiles Ri_g after $t = 5$ tend to converge toward the critical value 0.25 in the region where stirring occurs as shown in figure 5(*a*). The Ri_g profile at $t = 5$ shows that the region with $Ri_g < 0.25$ extends from the surface down to $z = -0.4$. The local minimum at $z = -0.75$ results from the maximum in the jet shear at that location as shown in figure 3(*b*). Stirring causes the entire surface layer and part of the jet upper flank to become linearly unstable, i.e. $Ri_g < 0.25$ as observed at $t = 20$. The $t = 20$ profile indicates three distinct regions: the thin viscous region, $-0.1 < z < 0$, in which Ri_g increases monotonically from the surface value; the stirring region, $-0.9 < z < -0.1$, in which Ri_g is maintained in a narrow band, $0.175 < Ri_g < 0.25$, of near-critical values; and the quiescent region, $z < -0.9$, where Ri_g becomes larger than 0.25 and sharply increases toward infinity (due to zero shear at the centre of the jet). At $t = 30$ and 45, the stirring region deepens and the Ri_g values in this region move closer to the critical value of $Ri_g = 0.25$ as stirring subsides. Recall the shear and squared buoyancy frequency profiles in figures 3(*b*) and 4(*b*), respectively. Locally, i.e. at different depths, the shear S can increase or decrease in time; nonetheless, mixing alters the squared buoyancy frequency accordingly such that Ri_g converges toward the critical value. The convergence of Ri_g toward the critical value along with the eventual decay of stirring suggests that the core dynamical process in the current study is shear instability according to linear stability theory. The convergence to $Ri_g \approx 0.25$ after $t = 20$ substantiates the typical use of $Ri_g > 0.25$ as a cutoff
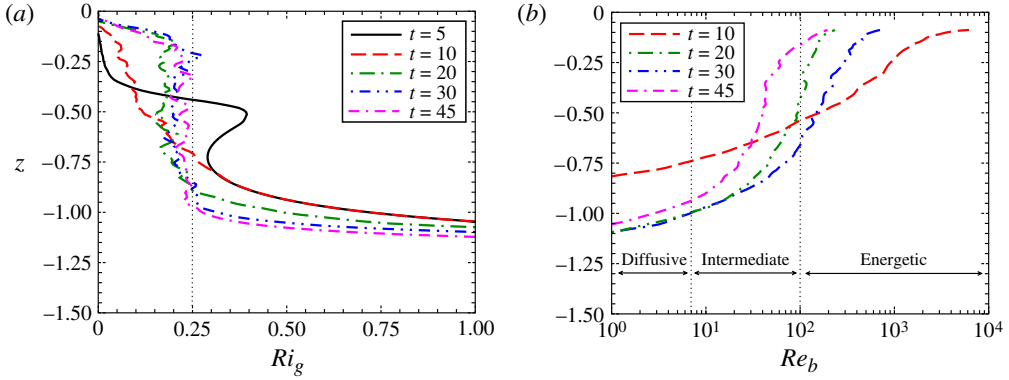
FIGURE 5. (Colour online) Vertical profiles of (*a*) the vertical gradient Richardson number Ri_g and (*b*) the buoyancy Reynolds number Re_b at various time. The dotted line in (*a*) indicates the critical value of Ri_g for linear shear instability. The regimes in (*b*) correspond to Shih *et al.* (2005).

for turbulent mixing in many environmental models. However, the significant mixing between $t = 5$ and $t = 10$ would be missed by such a simple mixing model. As the values of Ri_g increase toward 0.25, the turbulence intensity decreases. Figure 5(*b*) shows the profiles of the buoyancy Reynolds number, $Re_b = \varepsilon/(\nu N^2)$, a measure of turbulent mixing that has been investigated in simulations of homogeneous (Shih *et al.* 2005) and inhomogeneous (Pham & Sarkar 2010*b*) shear flows as well as analytical modelling (Galperin & Sukoriansky 2010). Between $t = 20$ and $t = 45$, the turbulence intensity in the region $-0.75 < z < -0.25$ decreases from the energetic regime to the intermediate regime according to the definition used by Shih *et al.* (2005) although the values of Ri_g do not vary significantly.

4. Internal waves

In the previous section, we have shown that mean background conditions have changed throughout the simulation indicating significant transfer between mean and fluctuating fields. In the current investigation, the fluctuating quantities can signify the presence of either internal gravity waves or turbulence or both. In this section, we present observations of the internal waves field that, excited by the wind-driven surface layer, propagates across the region with background jet shear.

Figure 6(*a–d*) shows snapshots of the instantaneous fluctuating vertical velocity field w' in the *x–z* plane at $y = 1.1$ at various times. In all plots, two distinct regions are observed: the turbulence region above and the wave region below. The region with turbulence shows small-scale fluctuations corresponding to high wavenumber while the wave region exhibits more coherent fluctuations which are at significantly larger wavelength. The wave regions have alternate black and white lobes in the horizontal direction corresponding to the negative wave troughs and the positive wave crests. As the simulation progresses, the turbulence layer penetrates to greater depth. The internal wave region changes noticeably in time. The wave field in figure 6(*a*) has smaller wavelength than those in other figures. The waves in figure 6(*b–d*) extend across the jet with the phase lines oriented in the vertical direction. Recall that the jet spans the region $-3 < z < -0.33$; the wave field in the region below the jet has phase lines that tilt upstream as shown in figure 6(*b,d*). The change in the propagating direction
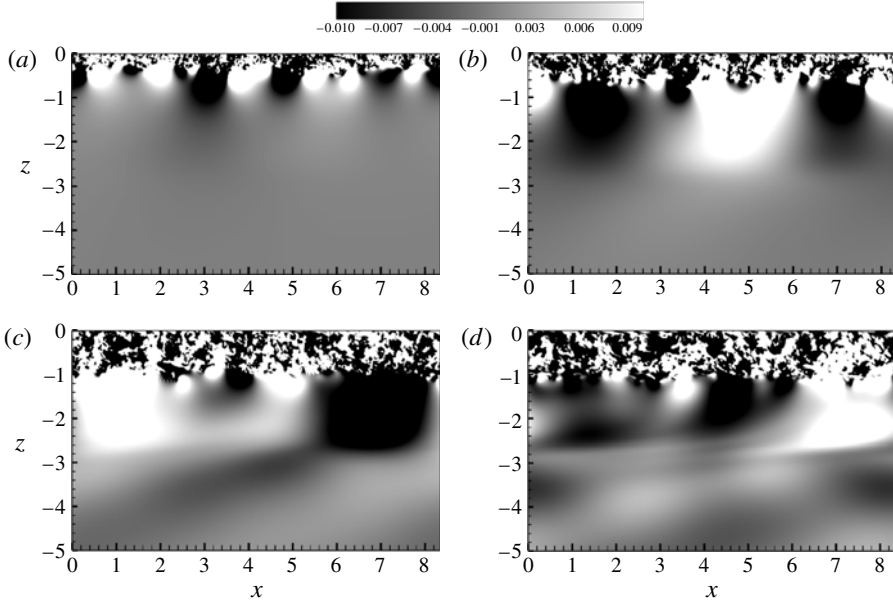
FIGURE 6. Internal wave fields are shown with the vertical fluctuating velocity field w' in the x–z plane at $y = 1.1$: (*a*) $t = 5$; (*b*) $t = 10$; (*c*) $t = 20$ and (*d*) $t = 30$.

of the wave phase lines is due to the change in the background shear. Similar to observations in the study of Pham & Sarkar (2010*a*) in which the vertical wavenumber m of the internal waves is governed by the Taylor–Goldstein equation, m is dependent on the horizontal wavenumber k, the background shear S and stratification N^2. In the region below $z = -1.25$ where N^2 is constant but the jet shear S varies with depth, the vertical wavenumber m also varies with depth resulting in the change in the wave phase lines.

In a previous study, Pham *et al.* (2009) reported that the internal waves excited by Kelvin–Helmholtz rollers have wavelength equal to that of the rollers. Pham & Sarkar (2010*a*) further showed that, in the presence of a stratified jet with EUC-type shear and stratification, the rollers cannot excite internal waves since the background shear and stratification do not allow propagating waves with positive values of m. Nevertheless, internal waves with larger horizontal wavelength were observed inside and below the jet because the smaller wavenumber k has positive m such that waves propagate. In both studies, the excited waves were found to be closely related to the coherent structures in the unstable shear layer. The waves were nearly two-dimensional and could be described by linear wave theory. In the current study, while there is a stratified jet as in Pham & Sarkar (2010*a*), the coherent rollers are absent and replaced by broadband turbulence in the upper mixed layer. Nonetheless, the wave excitation mechanism has similarities. Although the turbulence in the surface layer is broadband, there exist fluctuations at low wavenumber k which in combination with appropriate background conditions results in positive m for propagating internal waves. Figure 7(*a*) shows the internal waves through the density isosurfaces of $\rho = 0.048$ and 0.144 at $t = 5$. Unlike in previous studies where the internal waves are two-dimensional, i.e. x–z plane waves, the wave field shown in the isosurface of $\rho = 0.048$ at $t = 5$ is highly three-dimensional with distinct crater-like structures rather than lines of wave crests
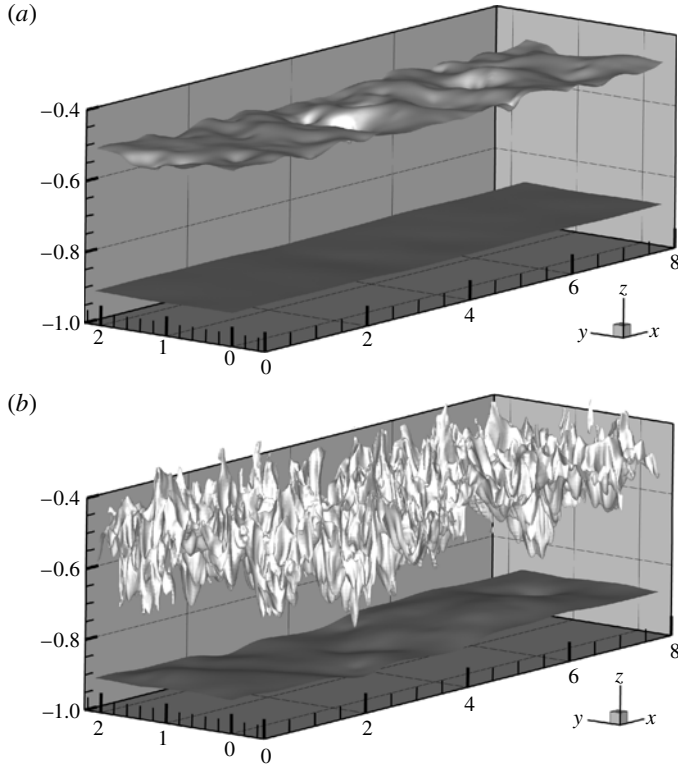
FIGURE 7. Internal waves are shown with 3D isosurfaces in the density field at (*a*) $t = 5$ and (*b*) $t = 10$. The lighter isosurface denotes $\rho = 0.048$ while the darker denotes $\rho = 0.144$.

and troughs. The three-dimensional features of the wave field suggest that these waves are correlated with the low-wavenumber fluctuation of the broadband turbulence in the region above. The isosurface of $\rho = 0.144$ shows no wave signature at early time. Figure 7(*b*) shows the same isosurfaces but at later time when the waves propagate toward greater depth. The waves shown in the isosurface of $\rho = 0.144$ have larger wavelength and smaller amplitude with fewer three-dimensional structures than those in the isosurface of $\rho = 0.048$ in figure 7(*a*). At $t = 10$, the isosurface of $\rho = 0.048$ shows the distinct features of turbulence especially in terms of larger amplitude and broader wavenumber spectrum than in the waves observed at $t = 5$.

The horizontally averaged k_x spectra of the streamwise velocity u' at $z = -0.33$ and -1 at various time are shown in figure 8(*a*,*b*), respectively. In figure 8(*a*), the spectrum at $t = 5$ is narrowband at low wavenumber and sharply drops off at wavenumber $k_x > 10$. At $t = 10$, the spectrum becomes broadband having the amplitude span 6 orders of magnitude with an energy containing range, an inertial subrange and a dissipation range indicative of turbulence. The peak magnitude in the spectrum at $t = 5$ is small suggesting that the internal waves present at this time are significantly weaker than the low-wavenumber fluctuations present during later time when there is broadband turbulence. Figure 8(*b*) shows similar evolution of the spectra at depth $z = -1$ inside the jet upper flank. The narrowband spectra at $t = 5$ and 10 are indicative of internal waves arriving from the surface layer above. At later time $t = 20$
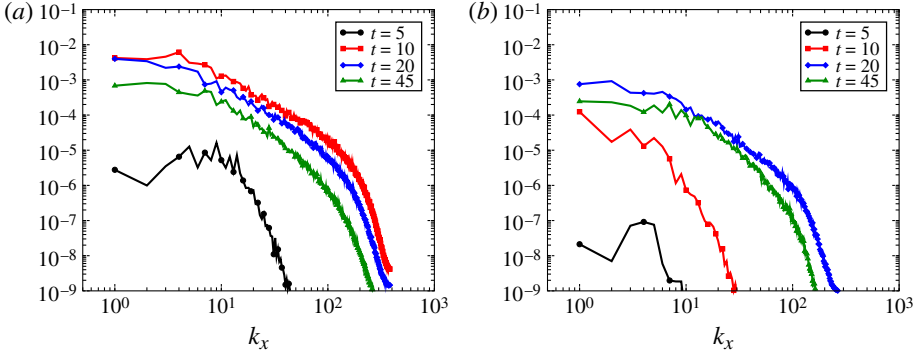
FIGURE 8. (Colour online) Spanwise averaged k_x spectra of the streamwise fluctuating velocity field u' at various times: (*a*) at $z = -0.33$ and (*b*) at $z = -1$.

and 45 the spectra become broadband and the turbulence is relatively weaker than that observed at similar time at $z = -0.33$.

While figure 8 shows that the peaks in the internal wave spectra are relatively smaller than those of the turbulence spectra, figure 9(*a–f*) further compares the magnitudes of the wave fluctuations with that of the turbulence fluctuations in terms of the r.m.s. values of streamwise velocity u', spanwise velocity v', vertical velocity w', density ρ', cross-correlation $\langle u'w' \rangle$ and pressure–velocity correlation $\langle p'w' \rangle$ at different times in the simulation. In these plots, there are two distinct regions: the turbulent region with larger fluctuations above (approximately $-1.25 < z < 0$) and the wave region with smaller fluctuations below (approximately $z < -1.25$). The peak velocity fluctuations in figure 9(*a–c*) in the turbulent region at $t = 5$, 10 and 20 are not at the surface, indicating that the major energy source for the fluctuations is the background shear, not the wind stress. When the mean flow is unstable, energy is extracted from the mean reservoir and deposited into the streamwise fluctuating velocity which in turn redistributes the energy to other components, i.e. spanwise and vertical, via pressure–strain correlations. The energy budget will be discussed thoroughly in § 7; here we continue to focus on the internal waves. The peak velocity fluctuations in figure 9(*a–c*) in the wave region are an order of magnitude smaller than those in the turbulent region. Thus, the fluctuating kinetic energy carried by the waves is significantly smaller compared to the turbulent kinetic energy present in the surface layer and upper portion of the jet. The wave fluctuations have larger u' and w' components than the v' components. The ρ' field shows a smaller difference between the wave and the turbulence region. It is noted that the location of the upper peak in ρ' indicate the approximate bottom boundary of turbulence and, thus, the stirring depth δ_s as discussed in the previous section. The lower peak in ρ' occurs at the location of maximum shear in the lower flank where there is internal wave reflection. The cross-correlation $\langle u'w' \rangle$ in the wave region is substantially smaller than that in the turbulent region and thus the momentum flux carried by the waves is insignificant compared to the turbulent Reynolds stress. The pressure–velocity correlation $\langle p'w' \rangle$, representative of the amount of fluctuating energy carried by waves, shows stronger downward energy transport at $t = 10$ compared to later time.

It is important to emphasize that the wave energy flux, T_p, in the current study is significantly weaker than turbulence transport, T_t, defined in (2.14). The vertical profiles of the three components of the transport term at $t = 10$ and $t = 20$ are plotted
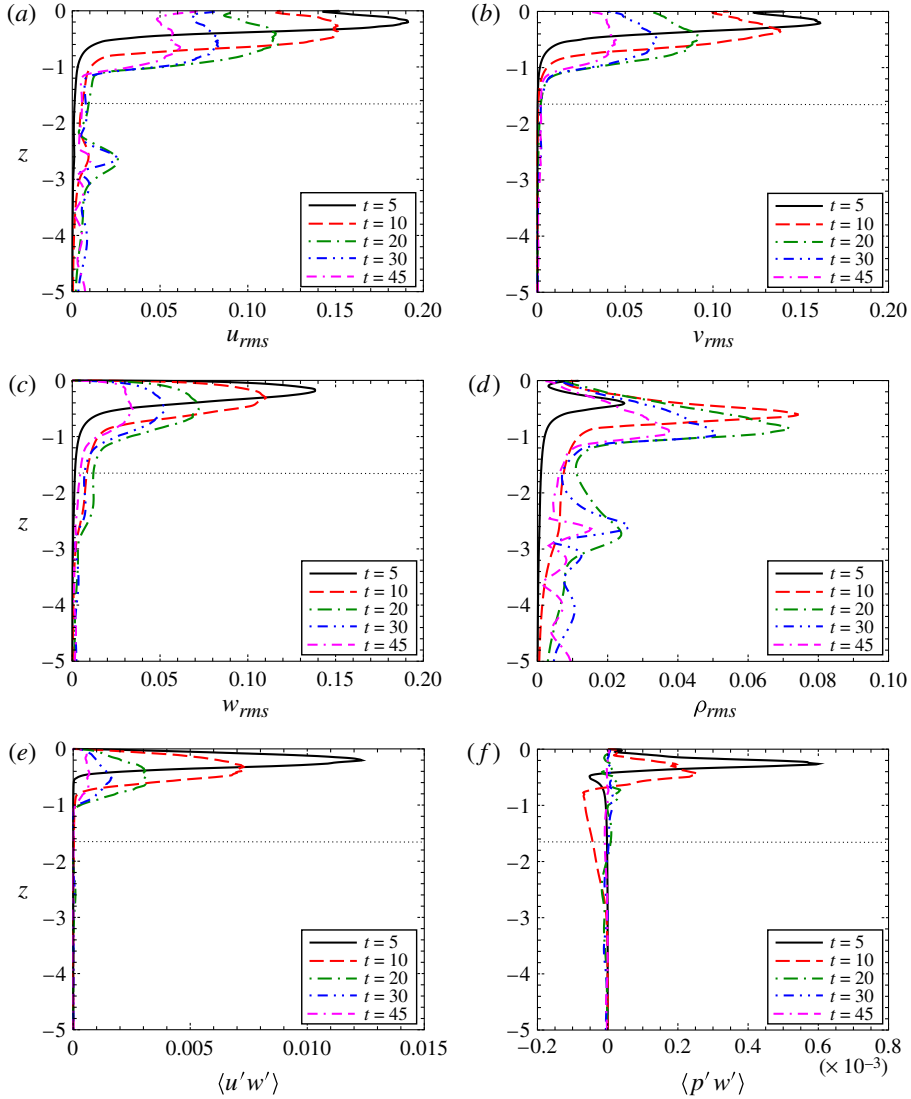
FIGURE 9. (Colour online) Horizontally averaged profiles of the fluctuating fields at various times: (*a*) streamwise velocity u_{rms}, (*b*) spanwise velocity v_{rms}, (*c*) vertical velocity w_{rms}, (*d*) density ρ_{rms}, (*e*) Reynolds stress $\langle u'w' \rangle$ and (*f*) wave energy flux $\langle p'w' \rangle$. The horizontal dotted lines indicate the centre of the jet. The upper zero-velocity point of the jet is at approximately $z = -0.4$ after $t = 10$.

in figure 10(*a,b*), respectively. In figure 10(*a*), the domain consists of two regions: the turbulence region above $z = -0.75$ in which T_t dominates the total transport and the wave region below $z = -0.75$ in which T_p, i.e. wave energy flux, dominates. In the turbulence region, T_t is positive in the surface layer indicating upward transport while T_t is negative in the jet upper flank denoting downward transport. In the wave region, the negative T_p indicates downward wave energy flux which is significantly smaller than the T_t values in the turbulence region. At later time, the turbulence region deepens to depth $z = -1.1$ as shown in figure 10(*b*). Both T_t and T_p are smaller than
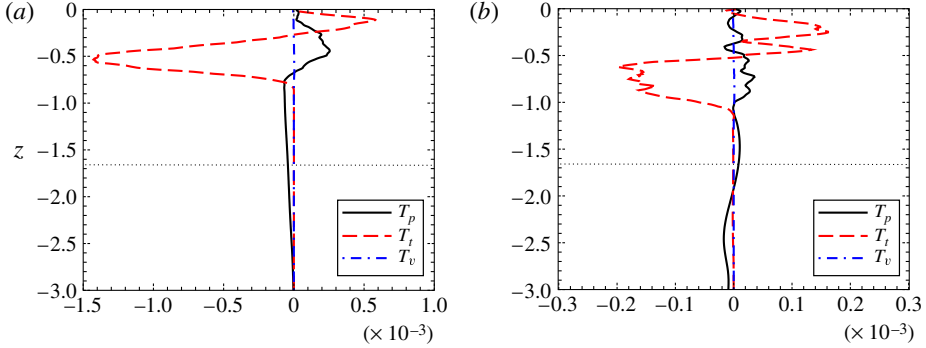
FIGURE 10. (Colour online) Contributions to the transport at (*a*) $t = 10$ and (*b*) $t = 20$. The
dotted lines indicate the centre of the jet.

the values at earlier time indicating weaker turbulent diffusion and weaker wave flux.
T_p changes sign across the centre of jet showing upward wave flux for the wave region
above. The reason is that some of the internal waves cannot penetrate past the lower
flank of the jet and thus reflect upward. Internal wave reflection due to changes in
the ambient velocity has been discussed by Brown & Sutherland (2007) and Pham &
Sarkar (2010*a*).

5. Mixing and generation of intermittent turbulence

As the surface layer deepens, we observe intermittent patches of turbulence in the
upper flank of the jet where the background gradient Richardson number is larger
than 0.25. In this section we examine the density field to elucidate the mixing
mechanisms leading to turbulence in the jet. The patches of turbulence are correlated
with the formation of gravitationally unstable density 'pockets'. The formation is due
to downward ejections in which lighter fluid is ejected downward into the quiescent
region with heavier fluid, upward ejections in which heavier fluid from the quiescent
region is ejected upward into the region with lighter fluid, and finally isopycnal
overturns. Evidence of these mechanisms is presented in the following text.

Downward ejections are evident in figure 11 which shows snapshots of the
instantaneous density field in the x–z plane at $y = 1.1$ at $t = 6.7$ and $t = 6.9$. In
figure 11(*a*), as the surface layer deepens the isopycnals in the interface region lying
between the turbulence region above and quiescent region below are distorted. The
distortions mainly consist of large-scale undulations. When the distortion has large
amplitude as in the region $3 < x < 5$, lighter fluid in the turbulence region extends
deep into the the quiescent region with significantly heavier fluid. The isopycnals at
the tip of the distortion at $x = 4.7$ and $z = -0.6$ in the circled region are compressed
against each other denoting stronger density gradients in both horizontal and vertical
directions compared to the ambient gradient. Figure 11(*b*) shows the subsequent
evolution of figure 11(*a*) at later time $t = 6.9$. The tip of the distortion shown in
figure 11(*a*) detaches from the isopycnal to evolve into individual 'pockets' of light
fluid surrounded by heavier fluid in figure 11(*b*). The 'pockets' are swept downstream
by the jet, i.e. the relative velocity is directed toward the positive x direction as they
are ejected downward.

Figure 12 illustrates upward ejections. As shown in the circled region in
figure 12(*a*), the fifth and sixth isopycnals from the bottom indicate the upward
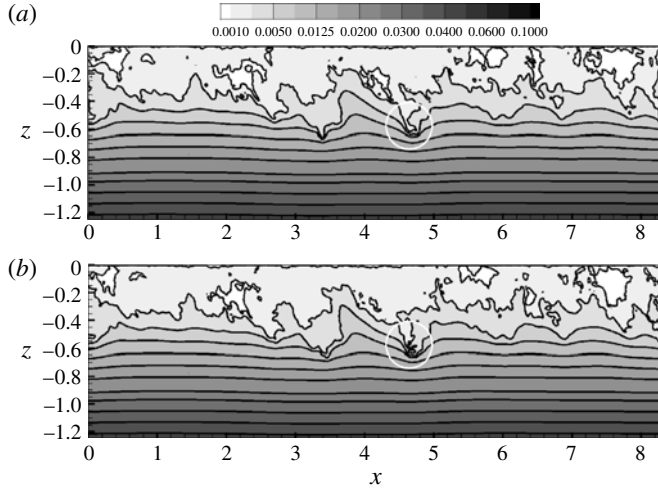
(a)

0.0010 0.0050 0.0125 0.0200 0.0300 0.0400 0.0600 0.1000

(b)

x

FIGURE 11. Downward ejection in the circled region is shown in vertical *x*–*z* slices of the density field at *y* = 1.1: (*a*) *t* = 6.7 and (*b*) *t* = 6.9.

(a)

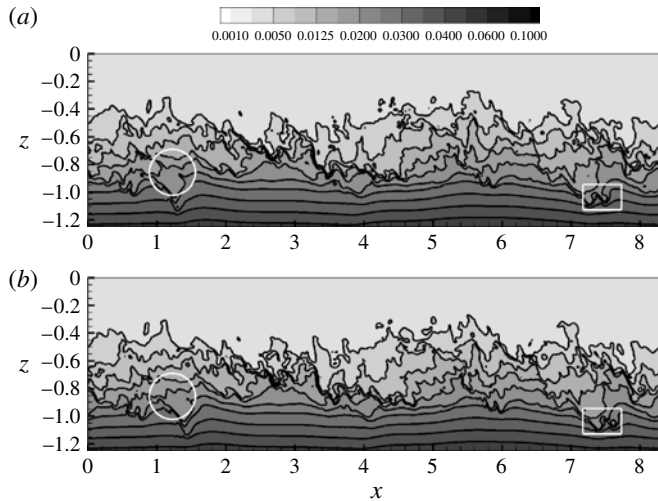0.0010 0.0050 0.0125 0.0200 0.0300 0.0400 0.0600 0.1000

(b)

x

FIGURE 12. Upward ejection in the circled region and isopycnal overturn in the rectanglular region are shown in vertical *x*–*z* slices of the density field at *y* = 1.1: (*a*) *t* = 18.7 and (*b*) *t* = 18.9.

ejection of heavier fluid in the region $1 < x < 1.5$. The ejections resemble finger-like structures pointing upstream, i.e. in the negative x direction. The ejections occur at depth $z = -0.9$ which is more than half of the total depth of the jet upper flank. In figure 12(*b*) which shows the subsequent evolution, the ejections are swept downstream by the jet velocity. The ejection in the sixth isopycnal from the bottom has disappeared; the ejection in the fifth isopycnal has evolved to become a separate 'pocket' surrounded by lighter fluid. The 'pocket' here is relatively smaller than those observed in the downward ejections, and it moves in the opposite direction. The orientation of the upward ejections is governed by the direction of mean spanwise
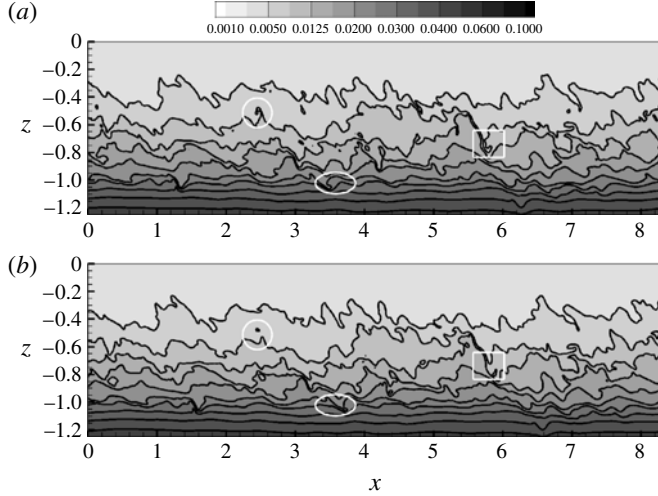
FIGURE 13. Upward ejection in the circled region, downward ejection in the rectangular region, and isopycnal overturning in the oval region are observed in vertical *x–z* slices of the density field at $y = 1.1$: (*a*) $t = 44.0$ and (*b*) $t = 44.3$.

vorticity ω_2. Since the background shear is negative and the positive y axis is directed into the page in figure 12, the negative ω_2 rotates fluid counter-clockwise and so do the upward ejections.

Figure 12 also presents evidence of isopycnal overturns in the rectangular region $7 < x < 8$. The fourth and fifth isopycnals from the bottom in figure 12(*a*) indicate two adjacent distortions which are about to overturn. The distortion to the right is of larger scale and the overturn direction is counter-clockwise. In figure 12(*b*), the distortions have been swept downstream and the one to the right has already overturned resulting a 'pocket' of light fluid surrounded by heavier fluid. The 'pocket' here is relatively larger than the one resulting from upward ejections.

The three mechanisms are presented again through snapshots at different times in figure 13 to emphasize their frequent occurrence in the jet upper flank. Figure 13(*a,b*) shows density contour plots near the end of the simulation at $t = 44.0$ and 44.3, respectively. Signatures of upward ejections are the abundant finger-like structures with counter-clockwise rotation in the isopycnals in the region $-0.8 < z < -0.4$. For example, the finger-like structure in the circled region in figure 13(*a*) at $x = 2.4$ and $z = -0.5$ is in the process of ejecting heavier fluid upward; the ejection is completed in figure 13(*b*) in which a 'pocket' can be seen. The downward ejection is observed in the rectangular region at $x = 5.7$ and $z = -0.8$. The second isopycnal from the top is distorted over a large vertical extent, $-0.8 < z < -0.5$, in figure 13(*a*). In figure 13(*b*), the bottom tip of the distortion detaches to become a separate 'pocket' which is advected further downward in the positive x direction. Finally, isopycnal overturn is evident as shown in the fifth isopycnal from the bottom in the oval region at $x = 3.5$. Figure 13(*a*) shows the distortion ready to overturn while figure 13(*b*) shows the completed overturn with a detached 'pocket'.

The drivers of the observed ejections are vortex tubes as shown in figures 14(*a,b*) and 15. In figure 14(*a*), three-dimensional isopycnal surface of $\rho = 0.144$ is used to visualize the downward ejection by a horseshoe-like vortex at $t = 18$. It is noted that the vertical axis has been flipped for visualization, i.e. up in physical space is directed

downward in the figure so that the surface layer is at the bottom of the figure. In figure 14(*b*), two isopycnal surfaces are shown: the darker corresponds to $\rho = 0.144$ which is shown in figure 14(*a*) while the lighter corresponds to $\rho = 0.197$. The ejection in the middle of the figure shows a horseshoe-like vortex originating from the darker surface extending toward the lighter surface. The vortex is swept slightly in the positive x direction as it penetrates upward in the figure (downward in physical space). A horseshoe-like vortex tube has been reported in Pham & Sarkar (2010*a*); however, there the vortex tube was a result of a secondary instability of a Kelvin–Helmholtz roller that interacted with the mean shear of a laminar jet. In figure 15, the three-dimensional features of the upward ejections are shown with the isopycnal surface of $\rho = 0.048$ at $t = 45$. The positive z axis is directed upward in this figure consistent with physical space. Unlike the one shown in figure 14, the horseshoe-like vortex labelled A extends upward and leans toward the negative x direction and it is in the process of breaking into two smaller tubes. Vortex tube labelled B shows a completed upward ejection of heavy fluid. Again, the ejection is upward and toward the negative x direction. The separated portion of the tube looks like a 'pocket' in the x–z plane.

Figure 16(*a*) shows the deepening of turbulence through a z–t diagram of density, analogous to a record taken by a density profiler, at fixed horizontal location, $x = 1.3$ and $y = 1.1$. The deepening occurs prior to $t = 20$ and penetrates to depth $z = -1$ which is well inside the jet upper flank. During the deepening, two downward ejections are observed: one at $t = 15$ and $z = -0.75$, and the other at $t = 18$ and $z = -1.1$. The ejections cause isolated short-lived dips in the density associated with fluid that is ejected downward. The second ejection penetrates to greater depth relative to the first. The dip due to the first ejection is seen in two consecutive isopycnals while the second ejection affects three consecutive isopycnals. After $t = 20$, the density shows continuous high-frequency fluctuations in region $-1 < z < -0.75$ in contrast to region $-1.25 < z < -1$ where the density exhibits intermittent dips corresponding to downward ejections of fluid, for example, at $t = 28$, 33 and 38. The ejections that occur after $t = 20$ are weaker than those that occur before with respect to the vertical penetration. The density fluctuations during this period do not deepen significantly causing the stirring depth δ_s to cease to increase as shown in figure 2(*b*). The corresponding z–t diagram of the dissipation at the same location is presented in figure 16(*b*). As the surface layer deepens, the turbulence region can penetrate as deep as $z = -1$ below which the dissipation rate sharply drops at least three orders of magnitude in a short vertical extent. The ejections in figure 16(*a*) are correlated with strong bursts of dissipation in figure 16(*b*). The bursts at $t = 15$ and 18 have dissipation at least three orders of magnitude larger than the surrounding values. The former burst causes strong dissipation, on the order of 10^{-3}, in the region $-1.2 < z < -1$ in which the gradient Richardson number Ri_g based on the mean profiles is significantly larger than 0.25 as shown in figure 5. It is evident that the dissipation observed in this region is not initiated by linear shear instability of the background mean flow. Rather, the dissipation is initiated by the penetration of horseshoe-like vortices from the region above that then interact with the background shear.

6. Momentum budget

In § 3 we have shown that the mean streamwise velocity $\langle u \rangle$ changes considerably throughout the simulations suggesting that the momentum budget of the jet has
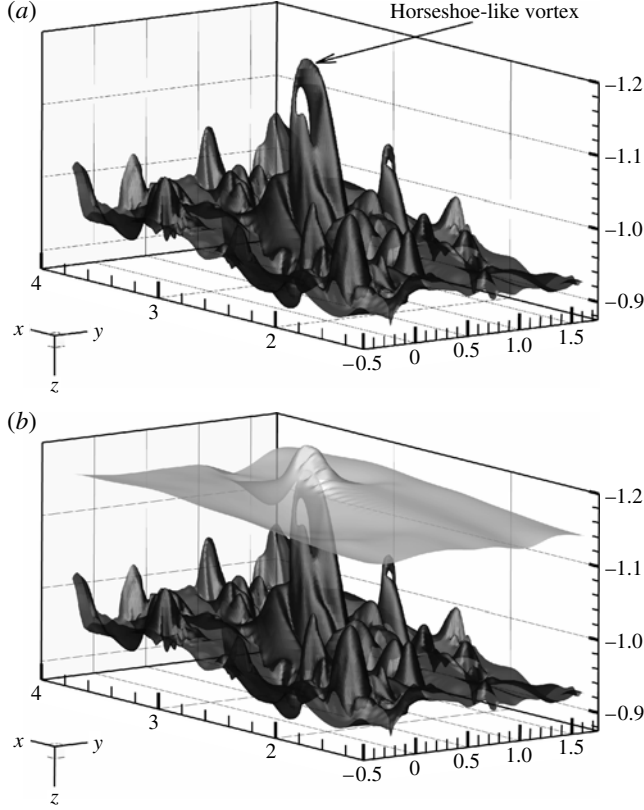
FIGURE 14. Ejections of light fluid are shown with 3D isocontours in the density field. Up in this figure corresponds to down in physical space. In (*a*), a horseshoe-like vortex tube ejects fluid from the stirring surface downward in physical space at $t = 18$. The ejection causes a localized region of density fluctuation in the jet in (*b*). The darker isosurface denotes $\rho = 0.144$ while the lighter one corresponds to $\rho = 0.197$. The negative z direction points upward in this figure.

changed in time. In this section, we analyse the momentum budget to show that the momentum loss inside the jet is due to the drag of the applied wind stress τ_w as well as the drag from the Reynolds stress $\langle u'w' \rangle$ extracted from the imposed mean shear in the surface layer, with the latter providing the dominant contribution.

Consider the horizontally averaged x-momentum equation after Reynolds decomposition:

$$\frac{\partial \langle u \rangle}{\partial t} = \frac{1}{Re} \frac{\partial^2 \langle u \rangle}{\partial z^2} - \frac{\partial \langle u'w' \rangle}{\partial z}. \tag{6.1}$$

Integrating the above equation from z_1 to z_2 yields

$$\underbrace{\frac{\partial}{\partial t} \int_{z_1}^{z_2} \langle u \rangle \, \mathrm{d}z}_{M_1} = \underbrace{\frac{S(z_2)}{Re}}_{M_2} - \underbrace{\frac{S(z_1)}{Re}}_{M_3} \underbrace{- \langle u'w' \rangle (z_2)}_{M_4} + \underbrace{\langle u'w' \rangle (z_1)}_{M_5}, \tag{6.2}$$
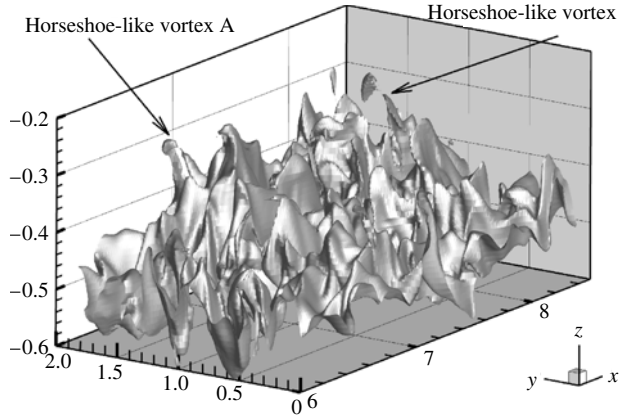
FIGURE 15. Ejections of heavy fluid are shown with 3D isocontours in the density field. Horseshoe-like vortex A is splitting into two smaller tubes. Broken vortex B shows a completed ejection of heavy fluid upward. The isosurface corresponds to $\rho = 0.048$ at $t = 45$.
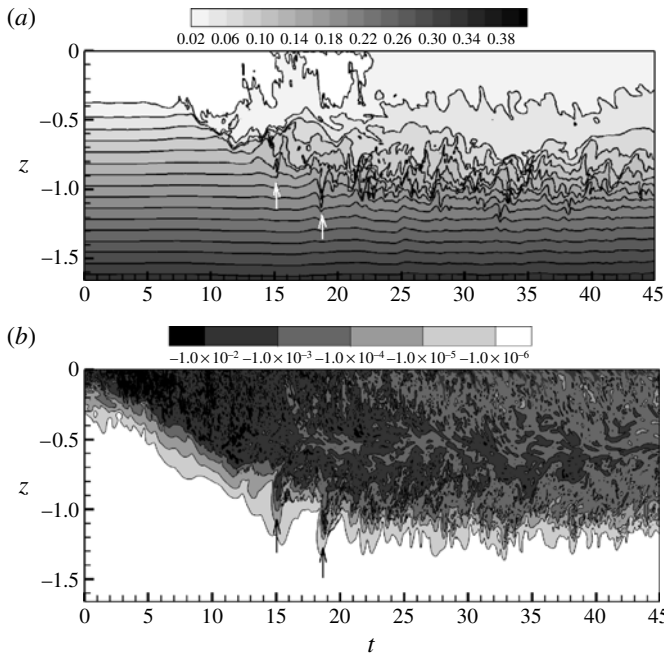

FIGURE 16. z–t diagrams of (a) the density field and (b) the dissipation field measured at $x = 1.3$ and $y = 1.1$. Arrows indicate the effect of downward ejections.

where S is used in place of $\mathrm{d}\langle u \rangle / \mathrm{d}z$. Equation (6.2) indicates the time rate of change of momentum inside a domain M_1 is equal to the net effect of viscous stresses, M_2 and M_3, and Reynolds stresses, M_4 and M_5.

Let us apply (6.2) to the surface layer with $z_1 = -0.33$ and $z_2 = 0$. Figure 17(a) shows the mean streamwise velocity $\langle u \rangle$ in the region at initial time $t = 0$ and at final time $t = 45$. In the region $-0.22 < z < 0$ the velocity magnitude decreases
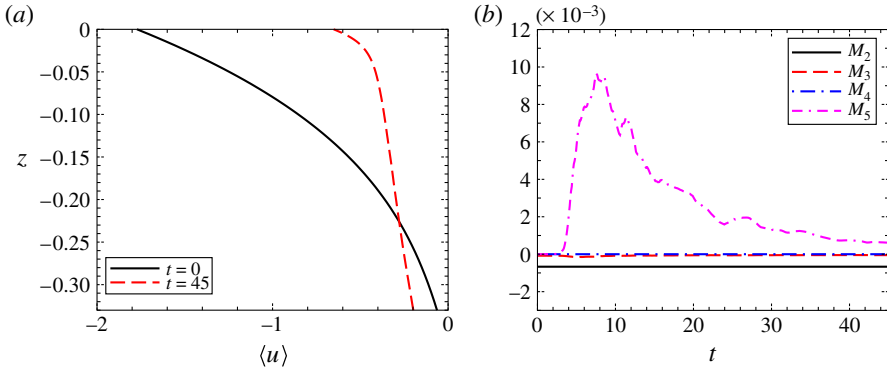
FIGURE 17. (Colour online) In the surface layer $-0.33 < z < 0$: (*a*) the initial and final mean streamwise velocity $\langle u \rangle$; (*b*) viscous drag, M_2 at $z = 0$ and M_3 at $z = -0.33$, and turbulence/wave drag, M_4 at $z = 0$ and M_5 at $z = -0.33$, as a function of time.

Domain	M_1	M_2	M_3	M_4	M_5
$-0.33 \leqslant z \leqslant 0$	0.098	−0.030	0.003	0.0	0.126
$-1.67 \leqslant z \leqslant -0.33$	−0.127	−0.003	0.0	−0.126	0.001

TABLE 2. Momentum budget: equation (6.2) integrated over the time of simulation.

considerably while it increases slightly in region $-0.33 < z < -0.22$ so that the surface layer exhibits a net loss of its initial (negative) momentum. The time evolution of the terms on the right-hand side of (6.2) is plotted in figure 17(*b*). At the surface $z_2 = 0$, M_2 is the applied wind stress τ_w taken to be constant in time. M_4 is equal to zero since no vertical velocity is allowed at the surface and M_3 is insignificant due to weak shear at z_1 as well as the large value of Re. The dominant term is M_5, the drag due to the Reynolds turbulent stress at z_1. M_5 increases sharply to its peak value during the early time when the background shear in the region is large. As the mean shear in the region decreases, M_5 also decreases. At the end of the simulation, the magnitude of M_5 is as small as that of the applied wind stress M_2. Integrating (6.2) over the time of simulation yields the bulk evolution of the momentum budget, and results are tabulated in table 2. Overall, the momentum loss in the background velocity M_1 is balanced by the wind drag M_2 at the surface and the turbulent drag M_5 at the bottom of the surface layer. Furthermore, M_5 is the largest term in the budget and it is the cumulative effect of both M_1 and M_2. In other words, the net turbulent drag at the base of the surface layer is the sum of the wind drag and the momentum extracted from the background velocity. The former is approximately 30 % of the latter as shown in table 2. Therefore, the background velocity provides a significantly larger contribution to the total drag than the wind stress.

Similar analysis is performed for the jet upper flank with $z_1 = -1.67$ and $z_2 = -0.33$. Figure 18(*a*) presents two profiles of the background velocity $\langle u \rangle$ at time $t = 0$ and 45. The difference between the two profiles indicates the momentum loss. Significant drag is observed in the top half of the jet upper flank; for example, the velocity at $z = -0.75$ is reduced by nearly half over the simulation. Figure 18(*b*) shows the time evolution of the terms on the right-hand side of (6.2). The viscous drag
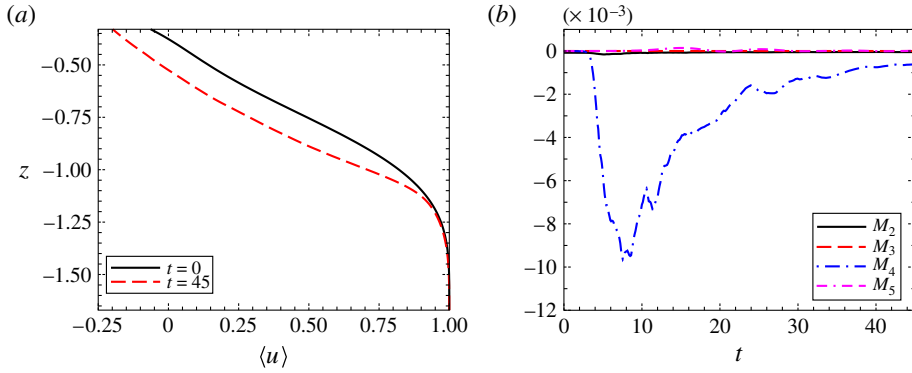
FIGURE 18. (Colour online) In the jet upper flank $-1.67 < z < -0.33$: (a) the initial and final mean streamwise velocity $\langle u \rangle$; (b) viscous drag, M_2 at $z = -0.33$ and M_3 at $z = -1.67$, and turbulence/wave drag, M_4 at $z = -0.33$ and M_5 at $z = -1.67$, as a function of time.

M_2 and M_3 are relatively small due to weak shear and large Reynolds number effect. The wave drag M_5, i.e. $\langle u'w' \rangle$, at the bottom of the region is small as discussed in §4. The only noticeable term is M_4 which is the drag due to the turbulent stress at the top of the jet. The results of integrating (6.2) in time are included on table 2 which indicates a direct balance between M_1 and M_4. The jet upper flank loses a significant amount of momentum due to the turbulent drag at the upper surface, $z_2 = -0.33$. The net momentum loss in the jet upper flank is 25 % larger than that in the surface layer. Combining the two analyses above yields the net effect of the wind stress and the initially imposed shear in the surface layer upon the jet. In bulk numbers, the wind stress contributes approximately 25 % of the total drag on the jet; the other 75 % is contributed by the background shear in the surface layer via turbulent extraction.

7. Kinetic energy budgets

Analysis of the momentum budget, given in the preceding section, indicates that the wind stress plays a smaller role in terms of momentum drag upon the jet than turbulent momentum fluxes in the subsurface sheared region. In this section, the budgets of the mean kinetic energy (MKE) and the turbulent kinetic energy (TKE) are examined to show that the mean energy input by the wind stress τ_w is also smaller than the amount of energy extracted from background shear. Also, the energy input by surface cooling is minuscule relative to the dominant terms in the TKE budget. Most of the energy lost to dissipation in the jet upper flank is localized to the region. The turbulent energy flux from the surface layer above provides a smaller net contribution but serves as an essential catalyst for mixing in the jet.

When (6.1) is multiplied by $\langle u \rangle$, the evolution equation for the MKE, K_m, is obtained:

$$\frac{\partial K_m}{\partial t} = \frac{\partial}{\partial z} \left[\langle u \rangle \left(\frac{S}{Re} - \langle u'w' \rangle \right) \right] - V - P, \quad (7.1)$$

where $K_m = (1/2)\langle u \rangle^2$, S is the shear rate, $V = S^2/Re$ is the viscous dissipation of the mean flow, and $P = -\langle u'w' \rangle S$ is the amount of MKE feeding into the turbulence. Integrating the above equation from the centre of the jet $z_j = -1.67$ to the surface
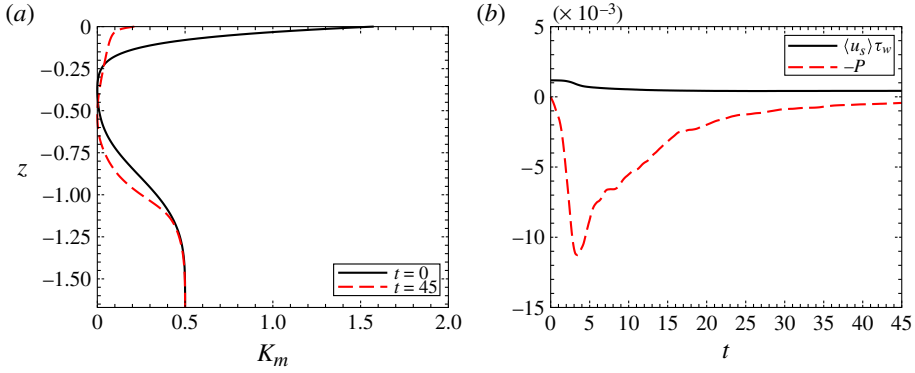
FIGURE 19. (Colour online) (*a*) Mean kinetic energy at $t = 0$ and 45; (*b*) energy input by the wind stress, $\langle u_s \rangle \tau_w$, and energy converted to turbulent kinetic energy P integrated over the region $-1.67 < z < 0$.

$z = 0$ yields

$$\frac{\partial}{\partial t} \int_{z_j}^{0} K_m \, dz = \langle u_s \rangle \tau_w - \int_{z_j}^{0} V \, dz - \int_{z_j}^{0} P \, dz, \qquad (7.2)$$

where the shear rate S at z_j and the Reynolds stresses $\langle u'w' \rangle$ at z_j and 0 are neglected. Equation (7.2) indicates two sources and two sinks for MKE during the simulation. The two sources are the energy available in the mean velocity at the initial time and the energy input by the wind stress. The two sinks are the viscous dissipation and the energy conversion to turbulent kinetic energy.

Figure 19(*a*) plots the vertical profiles of the MKE at the initial time $t = 0$ and the final time $t = 45$. The substantial difference between the two profiles indicates that a significant amount of the MKE is lost over the simulation especially in the surface layer. At the surface $z = 0$, despite continuous supply of energy by the wind, the MKE at the final time is 8 times smaller than that at the initial time. The jet upper flank also loses a considerable amount of MKE. Figure 19(*b*) contrasts the time evolution of the wind stress term and the production term on the right-hand side of (7.2). While the wind stress exerts a constant momentum drag over time upon the surface as discussed in the previous section, its energy input varies in time due to the decreasing surface velocity $\langle u_s \rangle$. The maximum energy input is at $t = 0$ and drops toward a constant at later time. The turbulence production term P is insignificant at time $t = 0$ but rises quickly to its peak followed by a decrease as the background shear decreases. The peak value of P is nearly 10 times larger than the peak energy input by the wind. At the end of the simulation, the two terms are approximately equal. Integrating the terms on the right-hand side of (7.2) over the time of the simulation gives the total energy input by the wind equal to 0.023 and the total energy converted to the TKE equal to -0.144. The left-hand side yields the total lost of MKE from the initially imposed background velocity equal to -0.13. Thus, the total amount of energy converted to the TKE is the sum of the energy input by the wind and the MKE lost from the mean velocity subtracting the relatively small viscous dissipation. The wind energy input only contributes 16 % of the energy converted to the TKE, and the reservoir of mean kinetic energy in the surface layer and the jet makes the major contribution.
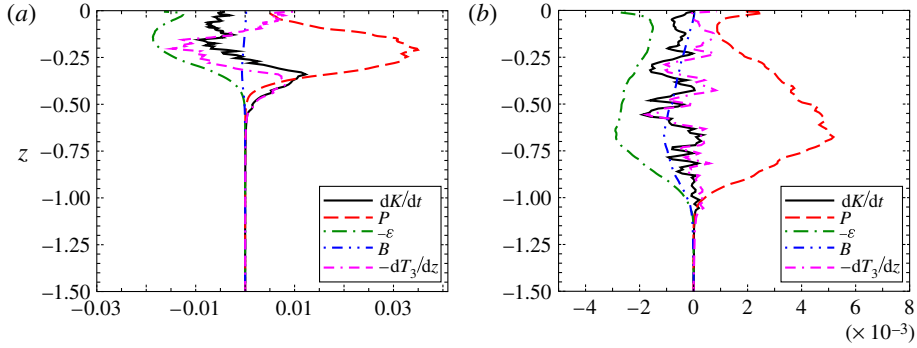
FIGURE 20. (Colour online) TKE budgets at (*a*) $t = 5$ and (*b*) $t = 20$.

Figure 20(*a,b*) plots the TKE budgets as described by (2.10) at $t = 5$ when the surface layer is deepening and at $t = 20$ when the deepening ceases, respectively. At $t = 5$ the dominant terms in the budget are the production P and the dissipation ε; the buoyancy flux B is small relative to other terms. The transport term consisting of both positive and negative values indicates that TKE is transported both upward and downward. Note that it is the negative of dT_3/dz that is plotted in figure 20. At the surface, TKE generated by the wind stress is transported downward. From $-0.35 < z < -0.1$, TKE is transported upward since a large amount of TKE is generated in the region of peak production. The peak production and dissipation occurs inside the sheared region, not at the surface, suggesting that more TKE is extracted from the mean shear than is input by the wind stress. At the base of the surface layer, positive dK/dt indicates TKE accumulation due to the downward negative energy transport. The production and dissipation at $t = 20$ in figure 20(*b*) are approximately an order of magnitude smaller than those at earlier time in figure 20(*a*). Over the surface layer and the jet upper flank, the production is balanced by the dissipation and the buoyancy flux. The peaks of the production and dissipation at $t = 20$ are further away from the surface when compared to those at $t = 5$ in figure 20(*a*). At the surface, the production locally peaks but the peak value is less than half of the peak value in the jet upper flank. Thus, even when the surface layer ceases to deepen, the larger energy input to the TKE budget is from the background shear in the jet, not from the wind stress.

Although the buoyancy flux B in figure 20(*a,b*) is smaller than the production and the dissipation, its magnitude is substantially larger than the surface cooling Q_s. Figure 21(*a*) shows vertical profiles of B normalized by Q_s at different times in the simulations in the surface layers. Near the surface $z = 0$, B carries positive sign denoting generation of TKE from potential energy. At the bottom portion of the layer, B changes to negative sign consistent with loss of TKE in stirring the background density. The magnitude of the negative B is significantly larger than that of the positive B at any time. Figure 21(*b*) illustrates the time evolution of B normalized by Q_s at different depths: $z = -0.05$ just outside the thin viscous layer, $z = -0.33$ at the base of the surface layer and $z = -1.1$ inside the jet upper flank. At $z = -0.05$, B has a positive value over the period $0 < t < 15$ with magnitude significantly larger than later values. The peak value of B occurs at $t = 3$ and is approximately 5 times larger than Q_s. At $z = -0.33$, B is negative over the entire simulation with the peak magnitude substantially larger than the value recorded at depth $z = -0.05$. Also, B at $z = -0.33$
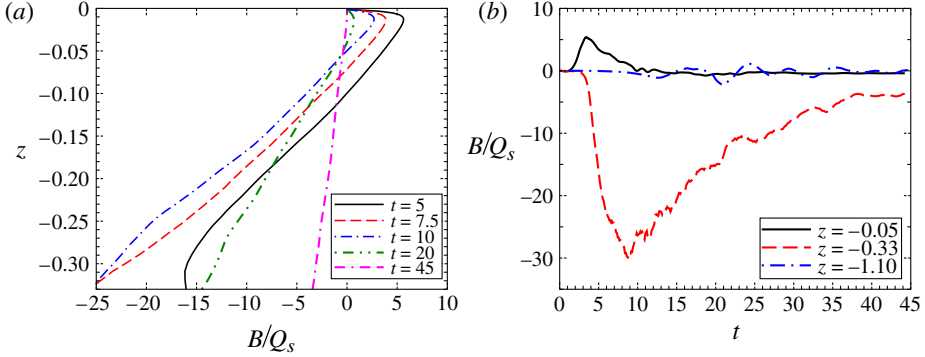
FIGURE 21. (Colour online) (*a*) Vertical profiles of the buoyancy flux *B* at various times; (*b*) the time evolution of *B* at different depths.
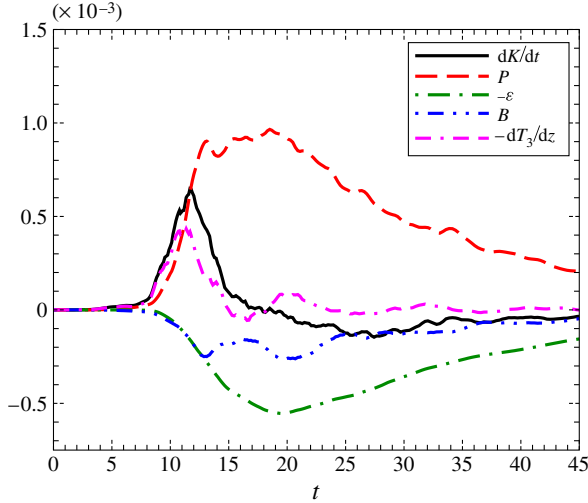

FIGURE 22. (Colour online) Integrated TKE budget over the upper flank of the jet $-1.67 \leqslant z \leqslant -0.33$.

is greater than Q_s at all times after $t = 3$. At $z = -1.1$, *B* has alternating signs with amplitude of order Q_s suggesting the presence of weak internal waves. The temporal and spatial evolution of *B* in figure 21(*a,b*) supports the notion that the energy input by surface cooling is minimal compared to the energy lost to stirring the background density, *B*, which in turn is significantly smaller than the turbulent production and dissipation.

To track the energy pathway to the turbulence observed in the jet upper flank, we integrate (2.10) across the region $-1.67 < z < -0.33$ to give the time evolution of the TKE budget, which is shown in figure 22. The evolution begins at $t = 7$ prior to which turbulence is contained in the surface layer. At $t = 7$, the dK/dt and transport terms rise followed later by a rise in the production. Therefore, at the beginning of the evolution, TKE is transported from the surface layer into the jet upper flank; only subsequently is energy extracted from the mean background jet shear. The peak
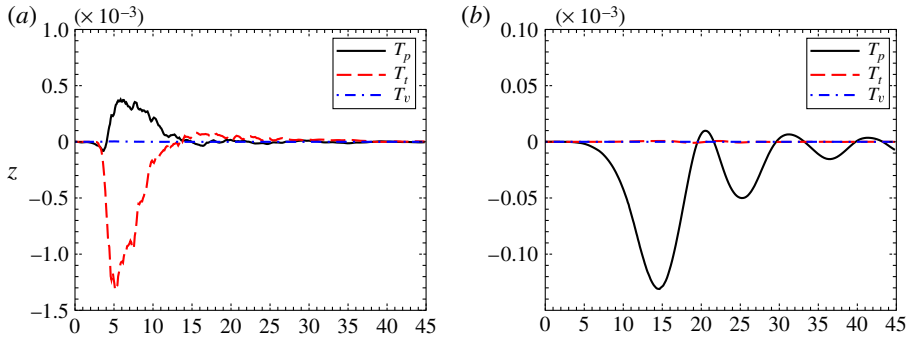
FIGURE 23. (Colour online) Amount of turbulent kinetic energy carried by the pressure transport T_p, turbulent transport T_t and viscous transport T_v across depth: (a) $z = -0.33$ and (b) $z = -1.67$.

downward transport that occurs at $t = 12$ is as large as 40 % of the peak production at $t = 19$. The downward transport continues until $t = 15$ after which for a period of time the transport direction is reversed, i.e. TKE is pumped from the jet back to the surface layer. During this period, the surface layer ceases to deepen and the production in the surface layer decreases to values smaller than the production in the jet as was shown in figure 20(b). Overall, the evolution shows that two sources of TKE are the production and transport while two sinks are the dissipation and buoyancy flux. Integrating the evolution over time gives the following values: net production of 0.02, transport of 0.0016, dissipation of -0.012, and buoyancy flux of -0.0049 and a surplus TKE of 0.0024 inside the jet upper flank at the end of the simulation. The production is more than 12 times larger than the transport indicating that the major source of TKE is local.

Although the net transport integrated over time is substantially smaller that the integrated production, the two term are comparable during the deepening of the surface layer $5 < t < 12$ as shown in figure 22. Therefore, it is important to identify which component of transports, i.e. T_p or T_t or T_v, is responsible for the energy delivery during deepening. The amount of energy transported by each component across the top boundary $z = -0.33$ and the bottom boundary $z = -1.67$ of the jet upper flank is plotted in figure 23(a,b), respectively. In figure 23(a), the viscous transport T_v is substantially smaller than the other components throughout the simulation. The pressure transport T_p begins to pump energy downward first via internal waves but quickly reverses direction at the same time that downward turbulent transport T_t commences. The peak downward T_t is more than three times larger than the peak upward T_p. Over the simulation, T_t is the largest component of transport, and therefore, TKE transported downward from the surface layer by turbulent diffusion is larger than that by internal waves. In figure 23(b), T_t is significantly smaller than T_p because there is no turbulence activity at the centre of the jet. Weak internal waves propagate across this depth toward the region below the jet. The peak value of T_p is approximately 10 times smaller than the peak of T_t in figure 23(a). The net result of the transport over the region $-1.67 < z < -0.33$ is an accumulation of TKE as discussed above. Even though the accumulation through the transport term is small compared to the production, it is the catalyst for turbulence extraction from the background shear. It should be emphasized that while wave energy enters the jet before turbulent transport by vortex structures, turbulence is not generated at that time, i.e. there is no

evidence of internal wave breaking. As soon as a small amount of turbulence arrives through turbulent transport, it triggers energy extraction from the background shear even though the gradient Richardson number of the mean flow is larger than 0.25.

8. Conclusions

In this study, we have examined internal waves and turbulence in a linearly stable stratified jet subject to the forcing of wind stress and surface cooling. The simulation begins with a symmetric jet situated below a surface shear layer driven by a constant wind stress. The surface layer is well mixed while the jet is stably stratified such that the gradient Richardson number inside the jet is larger than the critical value for linear shear instability.

Turbulence initiated by finite-amplitude broadband fluctuations is generated in the surface layer and deepens into the jet upper flank. Internal waves generated by the turbulent surface layer are observed to propagate downward across the jet. The wave momentum flux is significantly smaller than the Reynolds turbulent stress extracted from the background velocity. Similarly, the wave energy flux is insignificant compared to other terms in the balance of turbulent kinetic energy.

Intermittent patches of intense dissipation are observed inside the jet upper flank where the background gradient Richardson number is larger than 0.25. The dissipation in the patches is at least three orders of magnitude stronger than the ambient value. The patches are the result of ejections of fluid parcels. The ejections are observed to be directed both upward and downward and driven by the formation of horseshoe-like vortices.

Mixing leads to strong variation in both space and time of the mean shear, S, and the mean buoyancy frequency, N. Remarkably, the associated gradient Richardson number, $Ri_g = N^2/S^2$, evolves from both large and small values towards the critical value of $Ri_g = 0.25$ so that the region spanning the upper flank of the jet and the lower part of the surface layer is characterized by $Ri_g \sim 0.25$. The turbulent buoyancy flux, B, takes large negative values with magnitude as large as 30 times the surface buoyancy flux. The turbulent dissipation rate, ε, in the jet is significant, 3 orders of magnitude larger than the surface buoyancy flux. The subsurface mixing events lead to values of ε at locations deep in the upper flank of the jet that are comparable to the peak surface value at that time.

The momentum budget shows significant drag on the jet. The drag due to the wind stress is approximately a quarter of the drag caused by turbulent stress in the flow. The total energy input by the surface stress is 16% of the net amount lost in mean kinetic energy over the simulation. The constant energy input by surface cooling is insignificant compared to the turbulent production and dissipation in the surface layer at any time during the simulation.

The analysis of the TKE budget over the jet upper flank indicates that the major sources of turbulence in the region are the energy extraction from local mean shear and the downward turbulent transport from the surface layer. Turbulent transport occurs prior to turbulent production but is significantly smaller. Therefore, the role of surface forcing is to provide the finite-amplitude fluctuations that then draw energy from the background shear resulting in turbulence generation and intermittent patches of dissipation in the stratified jet.

The results from this study suggest an alternative explanation for the enhanced turbulence observed in the EUC. Linear stability analysis indicates that the EUC is stable when subject to infinitesimal perturbations; however, the EUC can be unstable

when exposed to finite-amplitude perturbations as in the current study. Vortices formed in the surface layer may extend into the EUC and act as finite-amplitude perturbations causing instability. It is also important to emphasize that the jet model in the current study does not accurately represent all the possibilities observed in the EUC jet. Internal wave breaking and shear instability can be the reasons for the enhanced turbulence when the jet model is varied parametrically. Parametric studies of jet models with more realistic forcing would be important in further understanding the dynamics in the EUC.

REFERENCES

BASAK, S. & SARKAR, S. 2006 Dynamics of a stratified shear layer with horizontal shear. *J. Fluid Mech.* **568**, 19–54.

BROWN, G. L. & SUTHERLAND, B. R. 2007 Internal wave tunnelling through non-uniformly stratified shear flow. *Atmos.-Ocean* **45**, 47–56.

BRUCKER, K. & SARKAR, S. 2007 Evolution of an initially turbulent stratified shear layer. *Phys. Fluids* **19**, 101105.

GALPERIN, B. & SUKORIANSKY, S. 2010 Geophysical flows with anisotropic turbulence and dispersive waves: flows with stable stratification. *Ocean Dyn.* **60**, 1319–1337.

GAYEN, B., SARKAR, S. & TAYLOR, J. R. 2010 Large eddy simulation of a stratified boundary layer under an oscillatory current. *J. Fluid Mech.* **643**, 233–266.

GREGG, M. C., PETERS, H., WESSON, J. C., OAKEY, N. S. & SHAY, T. J. 1985 Intensive measurements of turbulence and shear in the equatorial undercurrent. *Nature* **314** (14), 140–144.

HEBERT, D., MOUM, J., PAULSON, C. & CALDWELL, D. 1992 Turbulence and internal waves at the equator. Part ii: details of a single event. *J. Phys. Oceanogr.* **22**, 1346–1356.

LIEN, R.-C., MCPHADEN, M. & GREGG, M. 1996 High-frequency internal waves at 0°, 140° *w* and their possible relationship to deep-cycle turbulence. *J. Phys. Oceanogr.* **26**, 581–600.

MAHALOV, A., MOUSTAOUI, M., NICOLAENKO, B. & TSE, K. L. 2007 Computational studies of inertia-gravity waves radiated from upper tropospheric jets. *Theor. Comput. Fluid Dyn.* **21**, 399–422.

MOUM, J., HEBERT, D., PAULSON, C. & CALDWELL, D. 1992 Turbulence and internal waves at the equator. Part i: statistics from towed thermistors and a microstructure profiler. *J. Phys. Oceanogr.* **22**, 1330–1345.

PHAM, H. T. & SARKAR, S. 2010a Internal waves and turbulence in a stable stratified jet. *J. Fluid Mech.* **648**, 297–324.

PHAM, H. T. & SARKAR, S. 2010b Transport and mixing of density in a continuously stratified shear layer. *J. Turbul.* **24** (11), 1–23.

PHAM, H. T., SARKAR, S. & BRUCKER, K. A. 2009 Dynamics of a stratified shear layer above a region of uniform stratification. *J. Fluid Mech.* **630**, 191–223.

PHILANDER, S. 1980 The equatorial undercurrent revisited. *Annu. Rev. Earth Planet. Sci.* **8**, 191–204.

SHIH, L. H., KOSEFF, J. R., IVEY, G. N. & FERZIGER, J. H. 2005 Parameterization of turbulent fluxes and scales using homogeneous sheared stably stratified turbulence simulations. *J. Fluid Mech.* **525**, 193–214.

SKYLLINGSTAD, E. & DENBO, D. 1994 The role of internal gravity waves in the equatorial current system. *J. Phys. Oceanogr.* **24**, 2093–2110.

SMYTH, W. & MOUM, J. 2002 Shear instability and gravity wave saturation in an asymmetrically stratified jet. *Dyn. Atmos. Oceans* **35**, 265–294.

SMYTH, W. D., MOUM, J. N. & NASH, J. D. 2011 Narrowband oscillations in the upper equatorial ocean. Part II: properties of shear instabilities. *J. Phys. Oceanogr.* **41**, 412–428.

SUN, C., SMYTH, W. & MOUM, J. 1998 Dynamic instability of stratified shear flow in the upper equatorial pacfic. *J. Geophys. Res.* **103**, 10323–10337.

SUTHERLAND, B. R. 2006 Rayleigh wave-internal wave coupling and internal wave generation above a model jet stream. *J. Atmos. Sci.* **63**, 1042–1055.

SUTHERLAND, B. & LINDEN, P. 1998 Internal wave excitation from stratified flow over thin barrier. *J. Fluid Mech.* **377**, 223–252.

TAYLOR, J. R. & SARKAR, S. 2008 Stratification effects in a bottom Ekman layer. *J. Phys. Oceanogr.* **38**, 2535–2555.

TSAI, W., CHEN, S. & MOENG, C. 2005 A numerical study on the evolution and structure of a stress-driven free-surface turbulent shear flow. *J. Fluid Mech.* **545**, 163–192.

TSE, K. L., MAHALOV, A., NICOLAENKO, B. & FERNANDO, H. J. S. 2003 Quasi-equilibrium dynamics of shear-stratified turbulence in a model tropospheric jet. *J. Fluid Mech.* **496**, 73–103.

WANG, D., McWILLIAMS, J. & LARGE, W. 1998 Large-Eddy simulation of the diurnal cycle of deep equatorial turbulence. *J. Phys. Oceanogr.* **28**, 129–148.

WANG, D. & MULLER, P. 2002 Effects of equatorial undercurrent shear on upper-ocean mixing and internal waves. *J. Phys. Oceanogr.* **32**, 1041–1057.